


Ultralow electron-surface scattering in nanoscale metals leveraging Fermi-surface anisotropy

Sushant Kumar ¹, Christian Multunas ², Benjamin Defay ¹, Daniel Gall ¹ and Ravishankar Sundararaman ^{1,2,*}

¹*Department of Materials Science and Engineering, 110 8th St, Troy, New York 12180, USA*

²*Department of Physics, Applied Physics, and Astronomy, 110 8th St, Troy, New York 12180, USA*

 (Received 18 May 2022; revised 8 August 2022; accepted 11 August 2022; published 25 August 2022)

Increasing resistivity of metal wires with reducing nanoscale dimensions is a major performance bottleneck of semiconductor computing technologies. We show that metals with suitably anisotropic Fermi velocity distributions can strongly suppress electron scattering by surfaces and outperform isotropic conductors such as copper in nanoscale wires. We derive a corresponding descriptor for the resistivity scaling of anisotropic conductors, screen thousands of metals using first-principles calculations of this descriptor, and identify the most promising materials for nanoscale interconnects. Previously-proposed layered conductors such as MAX phases and delafossites show promise in thin films, but not in narrow wires due to increased scattering from side walls. We find that certain intermetallics (notably CoSn) and borides (such as YCo₃B₂) with one-dimensionally anisotropic Fermi velocities are most promising for narrow wires. Combined with first-principles electron-phonon scattering predictions, we show that the proposed materials exhibit 2–3× lower resistivity than copper at 5-nm wire dimensions.

DOI: [10.1103/PhysRevMaterials.6.085002](https://doi.org/10.1103/PhysRevMaterials.6.085002)

I. INTRODUCTION

Miniaturization of semiconductor integrated circuits leads to higher transistor density and performance [1–4], but computing performance beyond the 10-nm technology node is increasingly limited by RC delays in the nanoscale copper wires interconnecting the transistors [1,5,6]. The challenge stems from the dramatic increase of resistivity of metals when wire dimensions reduce below the electron mean free path λ (≈ 40 nm for copper [7]) due to surface and grain boundary scattering [5]. Several strategies are being actively investigated to address this bottleneck, including using metallic nanowires [8–11], doped multilayer-graphene-nanoribbons [12], two-dimensional metals [13], and topological semimetals [14–16] and insulators [17]. However, reliable interconnect materials that systematically outperform elemental metals like Cu remains a critical challenge.

Within the approximate semiclassical Fuchs-Sondheimer (F-S) [18,19] and Mayadas-Shatzkes (M-S) models [20] the resistivity of a polycrystalline square metal wire is

$$\rho = \rho_0 + \rho_0 \lambda \frac{3(1-p)}{4d} + \rho_0 \lambda \frac{3R}{2D(1-R)} \quad (1)$$

where ρ_0 is the bulk resistivity of the metal, d is the wire thickness, and D is the average grain diameter. (For thin films, replace $4d$ in the denominator of the second term by $8h$, where h is the film thickness [18,19], this model can be readily extended to account for rectangular wires and anisotropic mass tensors [21,22].) Here, surface specularity p and grain boundary reflectivity R are typically used as phenomenological

parameters to fit measured resistivities that exhibit the characteristic $1/d$ increase with reducing dimensions [7,23,24].

Figure 1(a) shows the variation of resistivity as a function of square wire width for single crystals of several elemental metals as predicted by Eq. (1), assuming the worst-case diffuse limit $p = 0$ of surface scattering, using the bulk experimental resistivity ρ_0 and factor $\rho_0 \lambda$ calculated from first-principles [7]. [The final grain boundary term of Eq. (1) vanishes with $D \rightarrow \infty$ for single crystals.] Note that Rh [25], Ir [26], and Mo [5] have a higher ρ_0 than Cu, but their resistivity becomes lower than Cu for small enough wires because they have a smaller $\rho_0 \lambda$, which is a common prefactor in the resistivity increase due to both surface and grain boundary scattering. Additionally, Cu must be surrounded by a liner material to promote adhesion and prevent diffusion of Cu atoms into the surrounding dielectric. This reduces the cross section of Cu within the total space available for the wire [5,27], increasing the effective resistivity even more rapidly as shown in Fig. 1(a).

Consequently, interconnects in next-generation semiconductor devices require a material with low resistivity at nanoscale dimensions, in addition to being resistant to electromigration allowing thinner or no liners. High-throughput screening using first-principles calculations can be invaluable in identifying promising materials, but resistivity at nanoscale dimensions is too computationally expensive to predict directly for thousands of materials. Instead, $\rho_0 \lambda$ serves as a “resistivity scaling coefficient” within the F-S model that can be calculated rapidly from the Fermi velocities over the Fermi surface of the metal calculated using density-functional theory (DFT) [7]. Consequently, $\rho_0 \lambda$ has been used extensively as a descriptor to screen elemental metals [7], intermetallics [23], and MAX phases (metallic carbides and nitrides) [28–32]. The measured resistivity increase in epitaxial films of many

*sundar@rpi.edu

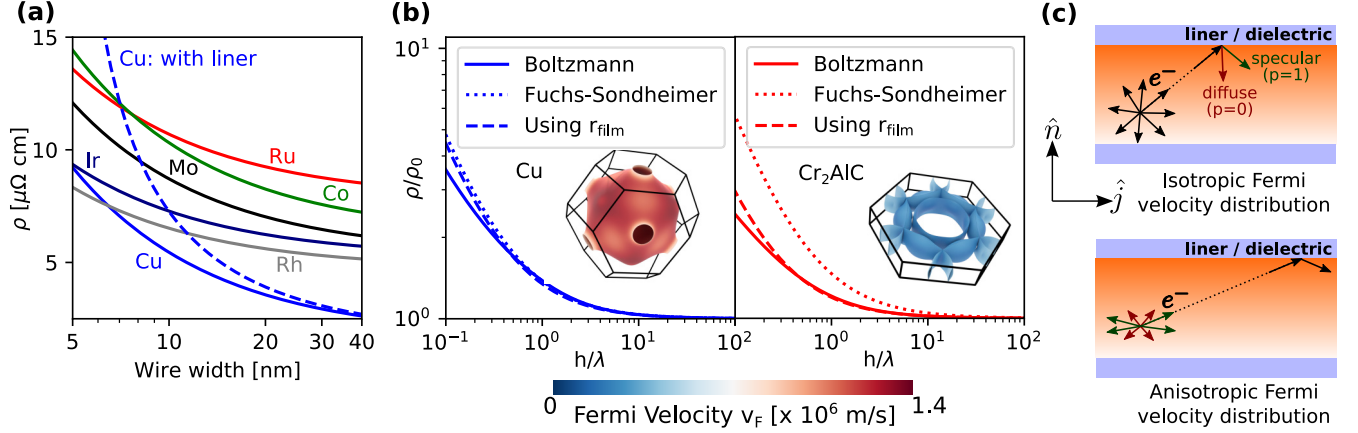


FIG. 1. (a) Resistivity increases with decreasing width of single-crystalline square wires due to increased surface scattering, shown here using the approximate Fuchs-Sondheimer (F-S) model [Eq. (1)] with $p = 0$ and $\rho_0\lambda$ calculated from first-principles [7]. The need for a liner for Cu (assumed 2-nm thick) reduces conducting cross section and increases resistivity further. (b) For isotropic conductors such as Cu, the F-S model is accurate compared to Boltzmann transport predictions for the increase of resistivity relative to bulk value ρ_0 with decreasing film thickness h compared to mean-free path λ , but it overestimates this effect for anisotropic conductors such as the Cr_2AlC MAX phase. Replacing $\rho_0\lambda$ with r_{film} derived here [Eq. (6)] fixes this discrepancy. (Insets show the corresponding Fermi surfaces.) (c) In anisotropic conductors, electrons with small velocity components encounter the surface less frequently, leading to the slower resistivity increase with reducing dimensions that we exploit here for new nanoscale interconnect materials.

elemental metals and intermetallics agree reasonably with calculated $\rho_0\lambda$ values [5,23,24], but they do not agree for highly anisotropic conductors. For example, in the Ti_4SiC_3 MAX phase material, the calculated $\rho_0\lambda$ is $5\times$ larger than the value extracted from measured resistance of epitaxial films [32]. This overestimation of the resistivity increase of anisotropic materials indicates that high-throughput materials screening using $\rho_0\lambda$ as a descriptor of nanoscale resistivity may miss promising candidates.

In this paper, we derive new resistivity scaling coefficients r_{film} and r_{wire} that capture the resistivity increase due to surface scattering in epitaxial thin films and wires of any material, fully accounting for anisotropy in excellent agreement with Boltzmann transport simulations. With a comparable computational cost to $\rho_0\lambda$, we are able to calculate these coefficients from first-principles for thousands of metallic materials to find the most conductive metals at nanoscale dimensions. We find promising candidates among several material classes including intermetallics, oxides and borides, which we investigate further using first-principles electron-phonon scattering simulations to identify the materials that can significantly outperform Cu in nanoscale wires.

II. ANISOTROPIC CONDUCTANCE DESCRIPTOR

We focus here on identifying the role of anisotropy in materials that outperform previous scaling predictions based on the $\rho_0\lambda$ descriptor, and restrict our attention to single-crystalline conductors where the resistivity increase is dominated by surface scattering (no grain boundaries). We begin by comparing the resistivity scaling for thin films of the nearly isotropic metal, Cu [7,33], and the highly anisotropic layered MAX phase conductor, Cr_2AlC [31,34,35], as limiting cases of interest in Fig. 1(b) with the Fermi surfaces shown as insets. The approximate F-S model predictions of ρ/ρ_0 agree with the Boltzmann transport simulations for Cu, except for extremely

thin films with thickness $h \ll \lambda$, the electron mean-free path. However, the F-S model strongly overestimates the resistivity increase in Cr_2AlC , for all h including $h \gg \lambda$.

To understand this discrepancy, consider the conductivity of crystalline thin films from the Boltzmann transport equation accounting for diffuse surface scattering and bulk electron-phonon scattering in the relaxation time approximation [18,36,37],

$$\sigma(h) = \sum_b \int_{\text{BZ}} \frac{e^2 g_s d\mathbf{k}}{(2\pi)^3} (-f'_0(\varepsilon_{\mathbf{k}b})) (\mathbf{v}_{\mathbf{k}b} \cdot \hat{\mathbf{j}})^2 \tau \times \left[1 - \frac{|\mathbf{v}_{\mathbf{k}b} \cdot \hat{\mathbf{n}}| \tau}{h} \left(1 - \exp \frac{-h}{|\mathbf{v}_{\mathbf{k}b} \cdot \hat{\mathbf{n}}| \tau} \right) \right] \quad (2)$$

where $\varepsilon_{\mathbf{k}b}$ and $\mathbf{v}_{\mathbf{k}b}$ are the electronic energies and velocities of band b and wavevector \mathbf{k} in the Brillouin zone (BZ), $g_s = 2$ is the spin degeneracy factor (neglecting spin-orbit coupling), and τ is the relaxation time. Above, the derivative $-f'_0(\varepsilon_{\mathbf{k}b})$ of the Fermi-Dirac occupations restricts contributions to within a few $k_B T$ of the Fermi energy.

The terms on the first line of Eq. (2) depend only on velocities along the current direction $\hat{\mathbf{j}}$ and capture the bulk contribution to conductivity. The terms on the second line depend on velocities along the surface normal direction $\hat{\mathbf{n}}$ and account for surface scattering (assuming the diffuse $p = 0$ case here for simplicity). Intuitively, this factor accounts for the fact that electrons with velocities nearly parallel to the surface encounter the surface much less frequently, and hence are less likely to be scattered, than those with a significant normal velocity component [Fig. 1(c)]. In contrast,

$$\frac{1}{\rho_0\lambda} = \sum_b \int_{\text{BZ}} \frac{e^2 g_s d\mathbf{k}}{(2\pi)^3} (-f'_0(\varepsilon_{\mathbf{k}b})) \frac{(\mathbf{v}_{\mathbf{k}b} \cdot \hat{\mathbf{j}})^2}{|\mathbf{v}_{\mathbf{k}b}|} \quad (3)$$

depends on the $\hat{\mathbf{n}}$ velocity component only through the overall magnitude $|\mathbf{v}_{\mathbf{k}b}|$, and without an explicit $\hat{\mathbf{n}}$ dependence,

misses this critical physical effect. Consequently, $\rho_0\lambda$ misses the advantage of small $|\mathbf{v}_{\mathbf{k}b} \cdot \hat{\mathbf{n}}|$ in anisotropic conductors and overestimates the resistivity increase with reducing film thickness.

We therefore retain explicit dependence on velocities along the surface normal $\hat{\mathbf{n}}$ and asymptotically expand Eq. (2). For large $h \gg |\mathbf{v}_{\mathbf{k}b} \cdot \hat{\mathbf{n}}|\tau$, we can neglect the exponential in the final term of Eq. (2) to find $\sigma(h) \approx g_1(\hat{\mathbf{j}})\tau - g_2(\hat{\mathbf{j}}, \hat{\mathbf{n}})\tau^2/h$, with

$$g_1(\hat{\mathbf{j}}) \equiv \sum_b \int_{\text{BZ}} \frac{e^2 g_s d\mathbf{k}}{(2\pi)^3} (-f'_0(\varepsilon_{\mathbf{k}b})) (\mathbf{v}_{\mathbf{k}b} \cdot \hat{\mathbf{j}})^2 \quad (4)$$

and

$$g_2(\hat{\mathbf{j}}, \hat{\mathbf{n}}) \equiv \sum_b \int_{\text{BZ}} \frac{e^2 g_s d\mathbf{k}}{(2\pi)^3} (-f'_0(\varepsilon_{\mathbf{k}b})) (\mathbf{v}_{\mathbf{k}b} \cdot \hat{\mathbf{j}})^2 |\mathbf{v}_{\mathbf{k}b} \cdot \hat{\mathbf{n}}|. \quad (5)$$

From the above, the resistivity varies as $\rho(h) \approx \rho_0 + g_2(\hat{\mathbf{j}}, \hat{\mathbf{n}})/(g_1(\hat{\mathbf{j}})^2 h)$, which is equivalent to the F-S model for single-crystal thin films [Eq. (1) with $4d \rightarrow 8h$ and $D \rightarrow \infty$], but with $\rho_0\lambda$ replaced by

$$r_{\text{film}} \equiv \frac{8g_2(\hat{\mathbf{j}}, \hat{\mathbf{n}})}{3g_1(\hat{\mathbf{j}})^2}. \quad (6)$$

Figure 1(b) shows that using this new resistivity scaling coefficient r_{film} , instead of $\rho_0\lambda$ in the approximate F-S model agrees very well with the Boltzmann transport simulations for both isotropic Cu and anisotropic Cr₂AlC.

Note that the above derivation is based on the condition that $h \gg |\mathbf{v}_{\mathbf{k}b} \cdot \hat{\mathbf{n}}|\tau$. This estimate is expected to work for films much thicker than the mean free path λ , but not for very thin films. However, in the limit of $h \ll \lambda$, classical transport is as such inaccurate, so it is not useful to attempt a better approximation. Only explicit and computationally expensive quantum mechanical simulations would be able to accurately predict conductance in this limit. Nevertheless, Fig. 1(b) shows that the new model performs well even for films with $h \sim \lambda$, with noticeable deviations only seen for $h < \lambda/10$ where semiclassical Boltzmann transport is anyway no longer valid. Therefore, r_{film} is adequate as a descriptor of nanoscale resistivity increase for high-throughput screening of interconnect materials, regardless of the anisotropy of conduction.

Importantly, calculating r_{film} is of comparable computational cost to $\rho_0\lambda$, just requiring two integrals of Fermi velocities over the Fermi surface in Eqs. (4) and (5), instead of single one. We reiterate that the explicit dependence of $g_2(\hat{\mathbf{j}}, \hat{\mathbf{n}})$ on velocities along the surface normal is critical for capturing the effect of anisotropy. Notice that $g_2(\hat{\mathbf{j}}, \hat{\mathbf{n}})$ and r_{film} are not tensors and can depend sensitively on directions, even for a materials where symmetry requires tensors to be isotropic. Even for cubic Cu, $\rho_0\lambda = 6.7 \times 10^{-16} \Omega\text{m}^2$ in any direction, while r_{film} ranges from $(6.1 \text{ to } 7.2) \times 10^{-16} \Omega\text{m}^2$ depending on the directions of $\hat{\mathbf{j}}$ and $\hat{\mathbf{n}}$; only a perfectly spherical Fermi surface would lead to $r_{\text{film}} = \rho_0\lambda$ in all directions. Among the elemental metals, cubic tungsten is an extreme case with $\rho_0\lambda = 8.1 \times 10^{-16} \Omega\text{m}^2$ in any direction, while r_{film} ranges from $(4.6 \text{ to } 12.1) \times 10^{-16} \Omega\text{m}^2$ due to the highly

directional velocities stemming from the shape of the Fermi surface [37]. Due to this direction dependence, for each material, we find the combination of perpendicular directions, $\hat{\mathbf{j}}$ and $\hat{\mathbf{n}}$, that minimize r_{film} .

We can straightforwardly generalize the above results for thin films to the case of rectangular wires, where electrons can scatter from the side walls in addition to the top and bottom surfaces. We find that replacing $\rho_0\lambda$ in the F-S model [Eq. (1)] by

$$r_{\text{wire}} \equiv \frac{8(g_2(\hat{\mathbf{j}}, \hat{\mathbf{n}}_1)w + g_2(\hat{\mathbf{j}}, \hat{\mathbf{n}}_2)h)}{3g_1(\hat{\mathbf{j}})^2(w+h)}, \quad (7)$$

where $\hat{\mathbf{n}}_1$ and $\hat{\mathbf{n}}_2$ are the surface normals along the height h and width w directions respectively, analogously matches the asymptotic expansion of the Boltzmann transport solution for rectangular wires. (See Supplemental Material [38] for details). The additional constraint of side wall scattering leads to $r_{\text{wire}} \geq r_{\text{film}}$, with equality for a spherical Fermi surface. For copper, $r_{\text{film}} = 6.1 \times 10^{-16} \Omega\text{m}^2$ only increases slightly to $r_{\text{wire}} = 6.2 \times 10^{-16} \Omega\text{m}^2$ for square wires ($w = h$). However, for Cr₂AlC, $r_{\text{film}} = 3.4 \times 10^{-16} \Omega\text{m}^2$ increases substantially to $r_{\text{wire}} = 6.5 \times 10^{-16} \Omega\text{m}^2$ for square wires, as most of the advantage for films compared to $\rho_0\lambda = 8.0 \times 10^{-16} \Omega\text{m}^2$ seen in Fig. 1(b) is lost due to side-wall scattering for wires. Consequently, to minimize r_{wire} for optimal scaling for narrow wires, we need to find materials with velocities that are directional along a single $\hat{\mathbf{j}}$ direction, with small components along both remaining perpendicular directions, $\hat{\mathbf{n}}_1$ and $\hat{\mathbf{n}}_2$. Below, unless mentioned otherwise, we report r_{wire} for square wires, and find the combination of mutually perpendicular $\hat{\mathbf{j}}$, $\hat{\mathbf{n}}_1$ and $\hat{\mathbf{n}}_2$ that minimize r_{wire} .

III. METHODS

We use the open-source plane-wave density-functional theory, JDFTx [39], to perform DFT calculations with the Perdew-Burke-Ernzerhof exchange-correlation functional [40] of each material with structure obtained from Materials Project [41]. We use the nonrelativistic ultrasoft Garrity-Bennett-Rabe-Vanderbilt (GBRV) pseudopotentials that have been optimized and tested extensively for high-throughput calculations using 20 and 100 Hartree wavefunction and charge density cutoffs [42]. We use a \mathbf{k} -point sampling selected automatically such that the effective length of \mathbf{k} -sampled supercell exceeds 100 \AA in each dimension, and use a Fermi smearing of 0.1 eV.

We perform spin-polarized calculations for metals whose magnetic moments have been reported to be greater than of $0.05 \mu_B$ in the Materials Project database. We do not include spin-orbit coupling as it would be computationally prohibitive for this high-throughput search, and in any case, most candidates do not include heavy elements for which the effects of spin-orbit coupling would become pronounced. We also do not include corrections for localized d or f electrons, such as DFT + U that has previously been used in studies of individual materials shown here such as Cr₂AlC [43] and PdCoO₂ [44], because determining empirical parameters such as U consistently across such a large set of materials is not straightforward.

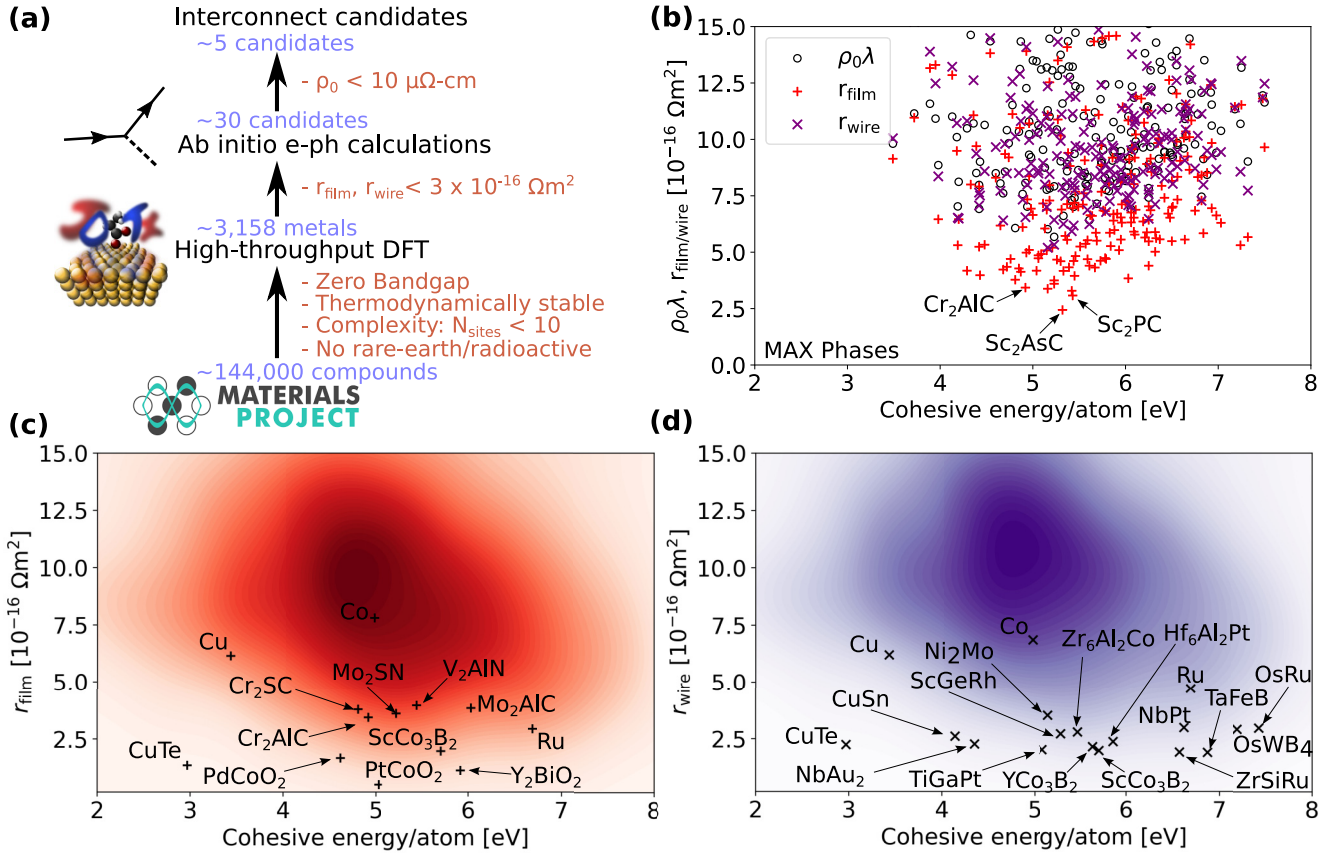


FIG. 2. (a) We filter stable earth-abundant metals using first-principles calculations of the resistivity scaling coefficients r_{film} and r_{wire} derived here [Eqs. (6) and (7)], and evaluate bulk resistivity ρ_0 for short-listed candidates using electron-phonon scattering calculations. (b) Anisotropic MAX phase conductors exhibit much lower resistivity increase in films given by r_{film} , than predicted by $\rho_0\lambda$, but lose this advantage in wires (higher r_{wire}). Most metals exhibit higher (c) r_{film} and (d) r_{wire} than Cu as shown by the probability density (using kernel density estimation) of the 3106 calculated values, but several intermetallic, oxide, and boride candidates (labeled) are lower than Cu. Cohesive energy on the x axis of [(b)–(d)] serves as a proxy for stability against electromigration (higher is better).

With electronic energies $\varepsilon_{\mathbf{k}b}$ and corresponding velocities $\mathbf{v}_{\mathbf{k}b}$ computed from the expectation value of commutator $-i[\mathbf{r}, \hat{\mathbf{H}}]/\hbar$ to account for nonlocal pseudopotential contributions [33], we directly evaluate the Brillouin zone (BZ) integrals in Eqs. (3), (4), and (5) on the fine DFT k mesh. We have benchmarked this direct BZ integration approach, which is more suitable for high-throughput calculations, against previous calculations of $\rho_0\lambda$ based on explicit Fermi surface constructions for several metals [7], and find excellent agreement as shown in Table S2 in the Supplemental Material [38]. For r_{film} and r_{wire} , we additionally identify the best combination of $\hat{\mathbf{j}}$, $\hat{\mathbf{n}}_1$, and $\hat{\mathbf{n}}_2$ to minimize these coefficients for each material. (This amounts to an optimization over 3×3 rotation matrices defined by these mutually-perpendicular unit vectors.)

For shortlisted materials, we perform first-principles electron-phonon scattering calculations to evaluate the bulk resistivity ρ_0 using JDFTx [39,45,46]. Briefly, we calculate phonons with a q -point mesh such that the effective length of the phonon supercell exceeds 15 Å in each dimension, and use maximally localized Wannier functions to interpolate electron, phonon and electron-phonon matrix elements to fine meshes exceeding 100 points in each dimension. We then compute the electron-phonon momentum relaxation time $\tau_{\mathbf{k}b}$

of each electronic state, and compute the bulk conductivity using the Boltzmann equation in the per-band relaxation time approximation. See Ref. [46] for details on the electron-phonon scattering calculation method.

IV. RESULTS

A. High-throughput screening

We use r_{film} and r_{wire} to search for the most conductive materials in thin films and narrow wires, starting from the Materials Project database with computed structures and electronic properties for over $\sim 144\,000$ compounds [41]. As indicated in Fig. 2(a), we first filter materials of interest based on properties already computed in this database. Zero band gap filters the number to $\sim 66\,000$ metals. Restricting to thermodynamically stable materials (energy within 0.02 eV of the convex hull to accommodate for DFT errors), excluding rare earth/radioactive elements, and focusing on materials with < 10 atoms per primitive unit cell (more complex unit cells are less likely to be reliably synthesized) brings this number down to 3106 candidates. We also include 214 MAX phase structures that are known for their layered structures and anisotropic electronic properties [34,35,47–51]. For all these 3320 structures, we perform DFT calculations of $\rho_0\lambda$, r_{film} ,

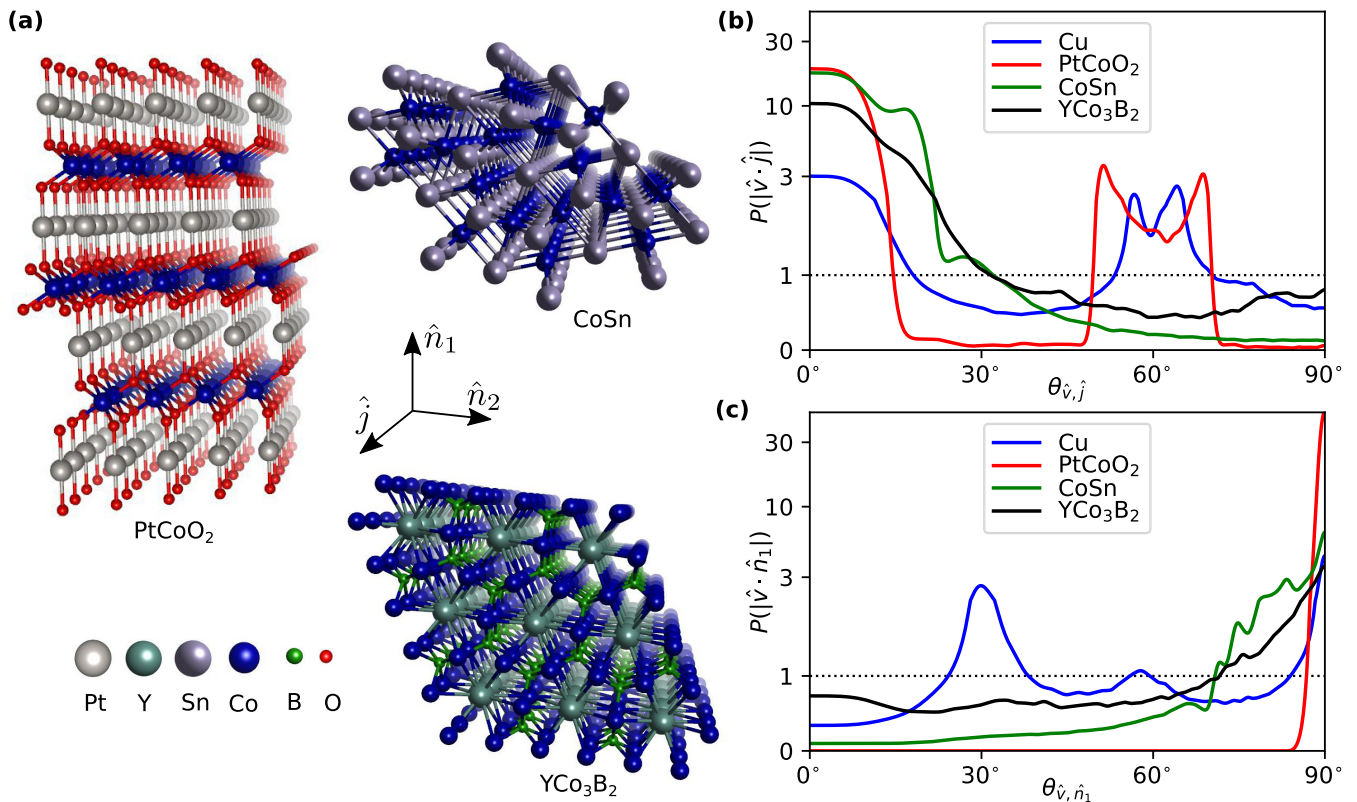


FIG. 3. (a) Crystal structures of the best candidates for low-resistivity thin films—PtCoO₂ and square wires—CoSn and YCo₃B₂, aligned to show the best transport direction \hat{j} , surface normal \hat{n}_1 , and side walls \hat{n}_2 (for wires). (b) The anisotropic conductors have much higher concentration of velocities near the transport direction, i.e., near $\theta_{\hat{v}, \hat{j}} = 0^\circ$, compared to Cu. (c) Correspondingly, the anisotropic conductors have higher concentration of velocities perpendicular to the surface normal, i.e., near $\theta_{\hat{v}, \hat{n}_1} = 90^\circ$. This leads to lower r_{film} and r_{wire} values, and hence lower expected resistivities at nanoscale dimensions.

and r_{wire} as detailed in the Methods section, and include a list of all calculated materials and properties in the Supplemental Material [38].

Figure 2(b) compares the predictions of $\rho_0\lambda$, r_{film} , and r_{wire} for all the MAX phase structures, plotted against the cohesive energy per atom, which measures the stability of the material and serves as a proxy for resistance against electromigration (higher is better). For all of these materials, the in-plane direction is strongly preferred for transport with $v_x, v_y \gg v_z$. Therefore, with \hat{j} in the xy plane and \hat{n} along z , the velocity components along \hat{n} are very small. This leads to $r_{\text{film}} \ll \rho_0\lambda$ as discussed above for Cr₂AlC. However, for the case of wires, we can only make the component of velocity along one of \hat{n}_1 and \hat{n}_2 small—whichever is along z —and the other component in-plane remains larger. Consequently, $r_{\text{wire}} \gg r_{\text{film}}$ and becomes comparable to $\rho_0\lambda$. Therefore, many of the MAX phases are expected to be excellent conductors in thin film geometries, but not in narrow wires necessary for semiconductor interconnects.

Figures 2(c) and 2(d) respectively plot r_{film} and r_{wire} against cohesive energy for all the metals shortlisted from Materials Project. They display a selection of the most promising candidates (low r values) along with the probability distribution of the 3106 calculated points, calculated using kernel density estimation. Most calculated materials have both r_{film} and r_{wire} larger than copper, we find ~ 30 promising candidates with

low values for at least one of r_{film} or r_{wire} . (In contrast, no material exhibits a lower $\rho_0\lambda$ than the best elemental metals.) The promising candidates also span different material classes, including intermetallics (CoSn, OsRu, CrNi₂, MoNi₂, and CuPt), borides (ScCo₃B₂, YCo₃B₂, and Mn₂B) and oxides (PdCoO₂ and PtCoO₂). Notably, two oxides with the delafossite structure—PdCoO₂ and PtCoO₂—exhibit $r_{\text{film}} = 1.66 \times 10^{-16} \Omega\text{m}^2$ and $0.50 \times 10^{-16} \Omega\text{m}^2$ respectively, the latter of which is $10\times$ lower than that of Cu. For square wires, we find 30 metals with r_{wire} less than $3 \times 10^{-16} \Omega\text{m}^2$ (\sim half that of copper) and five metals with r_{wire} less than $2 \times 10^{-16} \Omega\text{m}^2$ (\sim a third that of copper). (See Table S1 in the Supplemental Material [38] for a complete list of calculated properties.)

We next examine the connection between the resistivity scaling coefficients, structure and Fermi surfaces of materials, taking as examples the best film candidate, PtCoO₂, and the two best wire candidates, CoSn and YCo₃B₂, identified by our first-principles search above. Figure 3(a) shows the crystal structure of these three materials, oriented to indicate the best current direction and corresponding surface/side-wall normal directions. All three materials are hexagonal, but PtCoO₂ is layered with the best transport direction along the sheets of Pt atoms [52–54], while CoSn and YCo₃B₂ have the best transport direction down the line of Co atoms in each [55].

Figures 3(b) and 3(c) compare the distribution of velocity directions relative to the transport (\hat{j}) and normal (\hat{n}_1)

directions respectively on the Fermi surface of each of these anisotropic conductors, compared to Cu. A perfectly spherical Fermi surface would lead to probability density, $P(\cos \theta) = 1$, for angle θ measured to any axis. Cu is closest to this limit, while the anisotropic conductors focus their velocities along the transport direction ($\theta_{\mathbf{v}, \hat{\mathbf{j}}} = 0^\circ$) and perpendicular to the surface normal direction ($\theta_{\mathbf{v}, \hat{\mathbf{n}}_1} = 90^\circ$). For PtCoO₂, the velocities are restricted to a very small range of $\theta_{\mathbf{v}, \hat{\mathbf{n}}_1}$ near 90° [Fig. 3(c)], which leads to $r_{\text{film}} \ll \rho_0 \lambda$. However, the velocity angle distribution from the transport direction $\theta_{\mathbf{v}, \hat{\mathbf{j}}}$ peaks at both 0° and 60° in Figs. 3(b) due to the in-plane hexagonal symmetry. This leads to significant side-wall scattering and a high r_{wire} , analogous to the MAX phases discussed above. In comparison, the favored wire candidates, CoSn and YCo₃B₂ have the velocity direction distributions centered on $\theta_{\mathbf{v}, \hat{\mathbf{j}}} = 0^\circ$ as well as $\theta_{\mathbf{v}, \hat{\mathbf{n}}_1} = 90^\circ$, ensuring a low value of r_{wire} .

Figure 4 shows the Fermi surfaces of the above anisotropic conductors along with a few others with the lowest r_{wire} values (and that remain promising after accounting for bulk resistivity ρ_0 discussed next). In all cases, the Fermi surfaces exhibit almost flat surfaces perpendicular to the direction of current flow $\hat{\mathbf{j}}$, indicating that the Fermi velocity is along $\hat{\mathbf{j}}$ as shown previously in Fig. 3(b). The PtCoO₂ Fermi surface in particular is almost perfectly a hexagonal prism, with velocities almost perfectly in the xy plane that leads to the minuscule r_{film} (but unremarkable r_{wire}). The remaining Fermi surfaces in Fig. 4 for the wire candidates all exhibit multiple sheets normal to the $\hat{\mathbf{j}}$ direction, leading to the low r_{wire} that makes them promising for low-resistance wires.

It is important to note that, since our derivations of r_{film} and r_{wire} do not consider grain boundary scattering, the results of the high-throughput search presented here are limited to single-crystalline thin films and square wires. Previous studies have shown that the contribution of grain boundary scattering to increase in resistivity for smaller wires could be comparable in magnitude to that of the surface scattering [6,56]. Hence, an important direction for future research would be to devise new formalism, which could allow us to extend this high-throughput screening to polycrystalline films and wires [21,22].

B. Final selection by overall resistivity

The high-throughput screening so far using r_{film} and r_{wire} capture the increase of resistivity with reducing dimensions [in the second term of the F-S model, Eq. (1)]. A promising interconnect material should additionally exhibit low enough bulk resistivity ρ_0 that the overall resistance at some film or wire dimension is competitive compared to Cu. Consequently, the final stage in our computational screening [Fig. 2(a)] is the prediction of ρ_0 using first-principles electron-phonon scattering calculations (see Methods). Figure 5 shows the overall dimension-dependent resistivity of films and square wires for the most promising materials using the F-S model with both ρ_0 and r_{film} or r_{wire} calculated fully from first-principles, while Table I summarizes the calculated parameters for these candidates. The predicted resistivities agree well with measurements for known cases like Cu. The predicted mean free path for Cu (35 nm) also agrees reasonably with those extracted from experiment (40 nm), with the small discrepancy

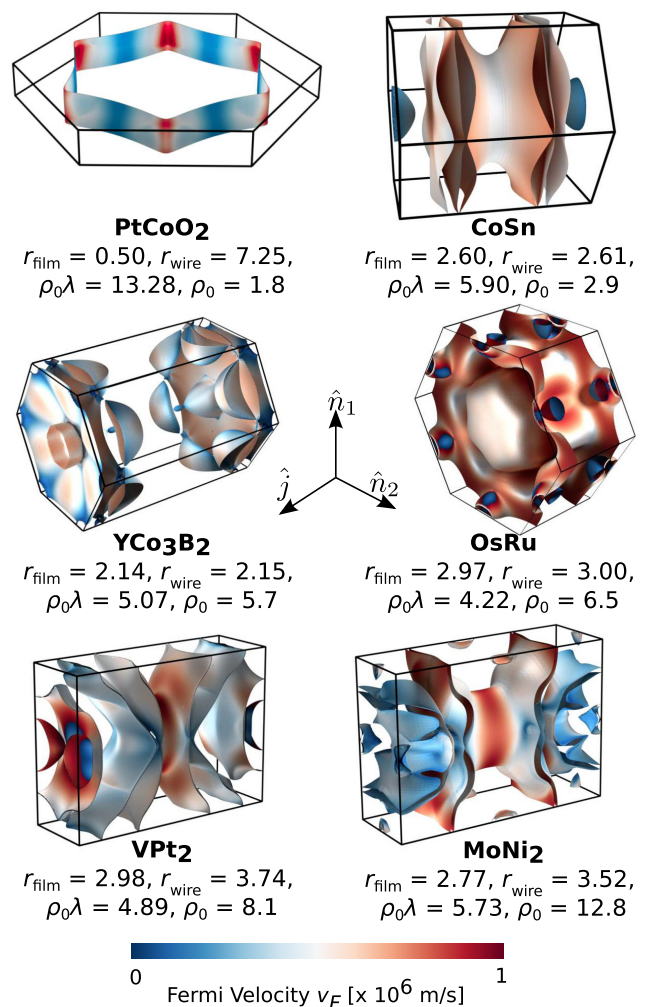


FIG. 4. Fermi surfaces of the best nanoscale conductors, short-listed by resistivity scaling coefficients r_{film} and r_{wire} (in $10^{-16} \Omega \text{m}^2$), and then filtered by bulk resistivity ρ_0 (in $\mu\Omega \text{cm}$) computed from first-principles. (Color indicates Fermi velocity magnitude.) All tend to have flat surfaces perpendicular to the best direction of current flow, leading to large Fermi velocities directed along the transport direction $\hat{\mathbf{j}}$ and much smaller velocity components along the surface normal $\hat{\mathbf{n}}_1$ and side wall $\hat{\mathbf{n}}_2$ directions (See Fig. S1 in the Supplemental Material [38] for Fermi surfaces of additional candidates).

because the experimental estimate assumes λ is constant on the Fermi surface [7], while the first-principles result explicitly accounts for this variation [33].

Figure 5 underscores the success of the new resistivity scaling coefficients in identifying candidates, which show unusually low increase in resistivity with decreasing thickness. Several shortlisted candidates like VNi₂, YCo₃B₂, CoSn, and PtCoO₂ exhibit a noticeable increase in resistivity only below 10 nm, especially for thin films [Fig. 5(a)]. Note that while several metals (e.g., VNi₂) show a slower resistivity increase than Cu, they lose the advantage because of their larger “baseline” resistivity ρ_0 and will only beat Cu at impractically small dimensions. Of the new candidates with low bulk resistivity ρ_0 , PtCoO₂ stands apart with ρ_0 and v_F comparable to Cu, while its r_{film} is an order of magnitude smaller, making it the

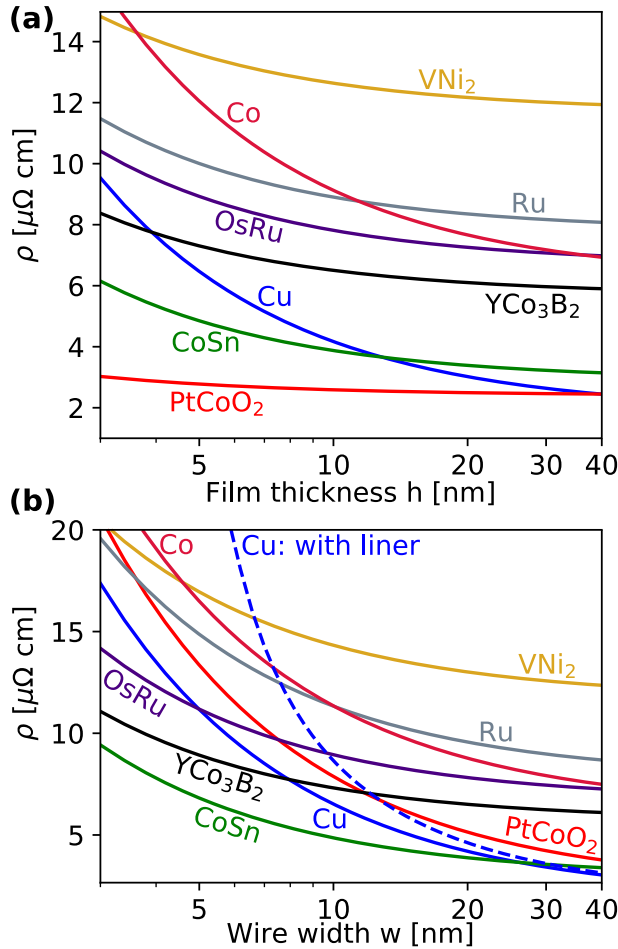


FIG. 5. Predicted electrical resistivity as a function of (a) film thickness and (b) square wire width for the best nanoscale conductors. PtCoO₂ is expected to outperform Cu for films thinner than 40 nm, while CoSn is expected to surpass Cu for films thinner than 13 nm as well as square wires narrower than 25 nm.

ideal material for thin films. However, as discussed above, it loses the advantage for wires due to side wall scattering.

For square wires relevant for interconnects, CoSn, YCo₃B₂, ScCo₃B₂, and OsRu promise to outperform Cu. Additionally, all these candidates have a cohesive energy greater than Cu, indicating the possibility that these materials are more stable against electromigration and could be usable without liners. Further, the ceramic candidates including the oxides and borides may exhibit better stability and surface properties than indicated by the cohesive energy alone. Figure 5(b) shows that the additional potential advantage in effective resistivity of these materials compared to Cu with a liner, if the new materials can be used without it. In particular, we expect CoSn to outperform Cu with a liner by 2× for 10 nm wires, and by 4× for 6 nm wires.

V. CONCLUSIONS

We have derived new descriptors of the increased resistivity of metals at nanoscale dimensions that account for

TABLE I. First-principles predictions of Fermi velocity v_F , electron mean free path λ , bulk resistivity ρ_0 , resistivity scaling coefficients $\rho_0\lambda$, r_{film} , and r_{wire} and cohesive energy per atom of promising candidates identified here, with the most promising cases among them highlighted. Note that ρ_0 and $\rho_0\lambda$ correspond to the best transport direction. See Supplemental Material [38] for complete listing, including specification of crystal orientations and other components of ρ_0 and $\rho_0\lambda$ tensors.

| Material | v_F [10 ⁶ m/s] | λ [nm] | ρ_0 [μΩ cm] | $\rho_0\lambda$ [×10 ⁻¹⁶ Ωm ²] | r_{film} | r_{wire} | Cohesive energy [eV/atom] |
|----------------------------------|--------------------------------|-------------------|---------------------|--|-------------------|-------------------|---------------------------------|
| Cu | 1.2 | 34.8 | 1.8 | 6.7 | 6.1 | 6.2 | 3.4 |
| Cr ₂ AlC | 0.3 | 5.6 | 14.5 | 8.0 | 3.4 | 6.5 | 4.9 |
| IrRu | 0.7 | 6.2 | 8.3 | 5.1 | 3.3 | 5.1 | 8.4 |
| CuPt | 0.8 | 11.2 | 6.1 | 6.8 | 3.3 | 5.1 | 4.6 |
| NiIr ₃ | 0.4 | 3.4 | 10.1 | 4.8 | 3.2 | 3.5 | 6.5 |
| VPt ₂ | 0.5 | 5.4 | 8.1 | 4.9 | 3.0 | 3.8 | 5.8 |
| IrRh | 0.7 | 5.8 | 6.6 | 3.6 | 3.0 | 3.5 | 6.4 |
| OsRu | 0.7 | 6.5 | 6.5 | 4.2 | 3.0 | 3.0 | 7.4 |
| MoNi ₂ | 0.4 | 5.7 | 12.8 | 5.7 | 2.8 | 3.5 | 5.2 |
| CrNi ₂ | 0.3 | 2.9 | 25.9 | 4.8 | 2.7 | 3.4 | 4.4 |
| CoSn | 0.6 | 19.6 | 2.9 | 5.9 | 2.6 | 2.6 | 4.4 |
| VNi ₂ | 0.3 | 3.9 | 13.9 | 4.5 | 2.5 | 3.5 | 5.0 |
| YCo ₃ B ₂ | 0.4 | 7.6 | 5.7 | 5.1 | 2.1 | 2.2 | 5.6 |
| ScCo ₃ B ₂ | 0.4 | 5.5 | 8.1 | 5.9 | 2.0 | 2.0 | 5.7 |
| PtCoO ₂ | 0.9 | 110.4 | 1.8 | 13.3 | 0.5 | 7.3 | 5.0 |

anisotropy and directionality of Fermi velocities. From first-principles evaluation of these descriptors for thousands of materials, we have identified new materials that can exploit this velocity directionality to potentially outperform copper significantly in interconnects for future semiconductor devices. In particular, we find PtCoO₂, which has recently attracted significant attention as a material with potential for hydrodynamic transport at low temperatures [57], to be the strongest candidate for thin films. For wires, intermetallics including CoSn and OsRu, as well as borides including YCo₃B₂ and ScCo₃B₂ are the most promising materials with velocities concentrated near a single transport axis, allowing them to simultaneously minimize scattering from top/bottom surfaces and side walls. Experimental validation of the predicted superior resistivity in nanoscale single-crystal films and wires, as well as computational understanding of the impact of defects and grain boundaries on the resistivity of directional conductors is necessary to realize the potential of these materials for future interconnects.

ACKNOWLEDGMENTS

The authors acknowledge funding from SRC under Task No. 2966. Calculations were carried out at the Center for Computational Innovations at Rensselaer Polytechnic Institute.

- [1] S. Salahuddin, K. Ni, and S. Datta, *Nat. Elec.* **1**, 442 (2018).
- [2] D. K. Ferry, *Science* **319**, 579 (2008).
- [3] K. Banerjee and A. Mehrotra, *IEEE Circuits Devices Mag.* **17**, 16 (2001).
- [4] H. K. Charles Jr, Johns Hopkins APL Tech. Dig. **26**, 402 (2005).
- [5] D. Gall, *J. Appl. Phys.* **127**, 050901 (2020).
- [6] D. Gall, J. J. Cha, Z. Chen, H.-J. Han, C. Hinkle, J. A. Robinson, R. Sundararaman, and R. Torsi, *MRS Bull.* **46**, 959 (2021).
- [7] D. Gall, *J. Appl. Phys.* **119**, 085101 (2016).
- [8] W.-H. Xu, L. Wang, Z. Guo, X. Chen, J. Liu, and X.-J. Huang, *ACS Nano* **9**, 241 (2015).
- [9] A. J. Simbeck, N. Lanzillo, N. Kharche, M. J. Verstraete, and S. K. Nayak, *ACS Nano* **6**, 10449 (2012).
- [10] N. A. Lanzillo, J. B. Thomas, B. Watson, M. Washington, and S. K. Nayak, *Proc. Natl. Acad. Sci. USA* **111**, 8712 (2014).
- [11] N. A. Lanzillo, *J. Appl. Phys.* **121**, 175104 (2017).
- [12] J. Jiang, J. Kang, W. Cao, X. Xie, H. Zhang, J. H. Chu, W. Liu, and K. Banerjee, *Nano Lett.* **17**, 1482 (2017).
- [13] Y. Hu, P. Conlin, Y. Lee, D. Kim, and K. Cho, *J. Mater. Chem. C* **10**, 5627 (2022).
- [14] C. Zhang, Z. Ni, J. Zhang, X. Yuan, Y. Liu, Y. Zou, Z. Liao, Y. Du, A. Narayan, H. Zhang, *et al.*, *Nat. Mater.* **18**, 482 (2019).
- [15] C.-T. Chen, U. Bajpai, N. A. Lanzillo, C.-H. Hsu, H. Lin, and G. Liang, in *2020 IEEE International Electron Devices Meeting (IEDM)* (IEEE, 2020), pp. 32.4.1–32.4.4.
- [16] H. J. Han, P. Liu, and J. J. Cha, *Matter* **4**, 2596 (2021).
- [17] T. M. Philip, M. R. Hirsbrunner, M. J. Park, and M. J. Gilbert, *IEEE Electron Device Lett.* **38**, 138 (2016).
- [18] K. Fuchs, *Math. Proc. Camb. Phil. Soc.* **34**, 100 (1938).
- [19] E. Sondheimer, *Adv. Phys.* **1**, 1 (1952).
- [20] A. Mayadas and M. Shatzkes, *Phys. Rev. B* **1**, 1382 (1970).
- [21] M. De Clercq, K. Moors, K. Sankaran, G. Pourtois, S. Dutta, C. Adelman, W. Magnus, and B. Sorée, *Phys. Rev. Materials* **2**, 033801 (2018).
- [22] S. Dutta, K. Moors, M. Vandemaale, and C. Adelman, *IEEE Electron Device Lett.* **39**, 268 (2018).
- [23] L. Chen, D. Ando, Y. Sutou, D. Gall, and J. Koike, *Appl. Phys. Lett.* **113**, 183503 (2018).
- [24] L. Chen, S. Kumar, M. Yahagi, D. Ando, Y. Sutou, D. Gall, R. Sundararaman, and J. Koike, *J. Appl. Phys.* **129**, 035301 (2021).
- [25] A. Jog, T. Zhou, and D. Gall, *IEEE Trans. Electron Devices* **68**, 257 (2020).
- [26] A. Jog and D. Gall, *J. Appl. Phys.* **130**, 115103 (2021).
- [27] A. E. Kaloyeros and E. Eisenbraun, *Annu. Rev. Mater. Sci.* **30**, 363 (2000).
- [28] B. D. Fahlman, in *Materials Chemistry* (Springer, New York, 2018), pp. 1–21.
- [29] M. Sokol, V. Natu, S. Kota, and M. W. Barsoum, *Trends Chem.* **1**, 210 (2019).
- [30] Z. Sun, *Int. Mater. Rev.* **56**, 143 (2011).
- [31] K. Sankaran, K. Moors, Z. Tókei, C. Adelman, and G. Pourtois, *Phys. Rev. Materials* **5**, 056002 (2021).
- [32] M. Zhang, S. Kumar, R. Sundararaman, and D. Gall, *J. Appl. Phys.* **130**, 034302 (2021).
- [33] A. M. Brown, R. Sundararaman, P. Narang, W. A. Goddard III, and H. A. Atwater, *ACS Nano* **10**, 957 (2016).
- [34] T. Ito, D. Pinek, T. Fujita, M. Nakatake, S.-i. Ideta, K. Tanaka, and T. Ouisse, *Phys. Rev. B* **96**, 195168 (2017).
- [35] T. Ouisse and M. W. Barsoum, *Mater. Res. Lett.* **5**, 365 (2017).
- [36] M. Lucas, *J. Appl. Phys.* **36**, 1632 (1965).
- [37] P. Zheng and D. Gall, *J. Appl. Phys.* **122**, 135301 (2017).
- [38] See Supplemental Material at <http://link.aps.org/supplemental/10.1103/PhysRevMaterials.6.085002> for derivation details, additional results, and complete tables of calculated properties for all materials.
- [39] R. Sundararaman, K. Letchworth-Weaver, K. Schwarz, D. Gunceler, Y. Ozhabes, and T. A. Arias, *SoftwareX* **6**, 278 (2017).
- [40] J. P. Perdew, K. Burke, and M. Ernzerhof, *Phys. Rev. Lett.* **77**, 3865 (1996).
- [41] A. Jain, S. P. Ong, G. Hautier, W. Chen, W. D. Richards, S. Dacek, S. Cholia, D. Gunter, D. Skinner, G. Ceder, and K. A. Persson, *APL Mater.* **1**, 011002 (2013).
- [42] K. F. Garrity, J. W. Bennett, K. M. Rabe, and D. Vanderbilt, *Comput. Mater. Sci.* **81**, 446 (2014).
- [43] M. Ramzan, S. Lebègue, and R. Ahuja, *Phys. Status Solidi (RRL)—Rapid Research Letters* **5**, 122 (2011).
- [44] C. W. Hicks, A. S. Gibbs, A. P. Mackenzie, H. Takatsu, Y. Maeno, and E. A. Yelland, *Phys. Rev. Lett.* **109**, 116401 (2012).
- [45] A. M. Brown, R. Sundararaman, P. Narang, W. A. Goddard III, and H. A. Atwater, *Phys. Rev. B* **94**, 075120 (2016).
- [46] A. Habib, F. Florio, and R. Sundararaman, *J. Opt.* **20**, 064001 (2018).
- [47] M. W. Barsoum and M. Radovic, *Annu. Rev. Mater. Res.* **41**, 195 (2011).
- [48] M. Higashi, S. Momono, K. Kishida, N. L. Okamoto, and H. Inui, *Acta Mater.* **161**, 161 (2018).
- [49] N. Haddad, E. Garcia-Caurel, L. Hultman, M. W. Barsoum, and G. Hug, *J. Appl. Phys.* **104**, 023531 (2008).
- [50] P. Yao, Y. Qian, W. Li, C. Li, J. Zuo, J. Xu, and M. Li, *Ceram. Int.* **46**, 22919 (2020).
- [51] G. Y. Khadzhai, R. Vovk, T. Prichna, E. Gevorkyan, M. Kislitsa, and A. Solovjov, *Low Temp. Phys.* **44**, 451 (2018).
- [52] V. Eyert, R. Frésard, and A. Maignan, *Chem. Mater.* **20**, 2370 (2008).
- [53] K. P. Ong, J. Zhang, J. S. Tse, and P. Wu, *Phys. Rev. B* **81**, 115120 (2010).
- [54] K. P. Ong, D. J. Singh, and P. Wu, *Phys. Rev. Lett.* **104**, 176601 (2010).
- [55] W. R. Meier, M.-H. Du, S. Okamoto, N. Mohanta, A. F. May, M. A. McGuire, C. A. Bridges, G. D. Samolyuk, and B. C. Sales, *Phys. Rev. B* **102**, 075148 (2020).
- [56] G. Hegde, R. C. Bowen, and M. S. Rodder, in *2016 IEEE International Interconnect Technology Conference/Advanced Metallization Conference (IITC/AMC)* (IEEE, 2016), pp. 114–116.
- [57] P. J. Moll, P. Kushwaha, N. Nandi, B. Schmidt, and A. P. Mackenzie, *Science* **351**, 1061 (2016).